12-2019

Comparison and Design Optimization of a Five-Phase Flux-Switching PM Machine for In-Wheel Traction Applications

Hao Chen

Xiangdong Liu

Nabeel Demerdash

Ayman M. EL-Refaie

Jing Zhao

See next page for additional authors

Authors
Hao Chen, Xiangdong Liu, Nabeel Demerdash, Ayman M. EL-Refaie, Jing Zhao, and Jiangbiao He

IEEE Transactions on Energy Conversion, Vol. 34, No. 4 (December 2019): 1805-1817. DOI.

Comparison and Design Optimization of a Five-Phase Flux-Switching PM Machine for In-Wheel Traction Applications

Hao Chen
School of Automation, Beijing Institute of Technology, Beijing, China
Xiangdong Liu
School of Automation, Beijing Institute of Technology, Beijing, China
Nabeel A. O. Demerdash
Department of Electrical and Computer Engineering, Marquette University, Milwaukee, WI
Ayman M. EL-Refaie
Department of Electrical and Computer Engineering, Marquette University, Milwaukee, WI
Jing Zhao
School of Automation, Beijing Institute of Technology, Beijing, China
Jiangbiao He

Department of Electrical and Computer Engineering, University of Kentucky, Lexington, KY

Abstract

A comparative study of five-phase outer-rotor flux-switching permanent magnet (FSPM) machines with different topologies for in-wheel traction applications is presented in this paper. Those topologies include double-layer winding, single-layer winding, C-core, and E-core configurations. The electromagnetic performance in the low-speed region, the flux-weakening capability in the high-speed region, and the fault-tolerance capability are all investigated in detail. The results indicate that the E-core FSPM machine has performance advantages. Furthermore, two kinds of E-core FSPM machines with different stator and rotor pole combinations are optimized, respectively. In order to reduce the computational burden during the large-scale optimization process, a mathematical technique is developed based on the concept of computationally efficient finite-element analysis. While a differential evolution algorithm serves as a global search engine to target optimized designs. Subsequently, multiobjective tradeoffs are presented based on a Pareto-set for 20 000 candidate designs. Finally, an optimal design is prototyped, and some experimental results are given to confirm the validity of the simulation results in this paper.

SECTION I. Introduction

With The ever-increasing demands for energy savings and environmental protections, the electric vehicle (EV), as a representative of clean-energy mobility options, is drawing more and more attention [1], [2]. Compared with the traditional EVs driven by differential gears, the directly driven EVs with in-wheel motors have many merits, e.g., higher control flexibility and higher transmission efficiency. However, the in-wheel traction concept raises the challenge for the motor design due to the constrained space and high torque density requirements [3].

Various types of motors have been considered for in-wheel traction applications. Switched reluctance motors (SRM) have led the way due to their rugged and simple construction, hazard-free operation, and ability of high-speed operation. However, they are facing a number of drawbacks, such as low power density, fairly high torque ripple and acoustic noise [4]. Induction motors are widely used due to their high reliability and low production cost. However, because of their low efficiency, low power factor, and low inverter-usage factor, induction motors are facing fierce competition from permanent magnet synchronous motors (PMSMs) [5]. In conventional PMSMs, e.g., surface-mounted PMSMs and interior PMSMs, the PMs are located on the rotor, which suffer from the risk of irreversible demagnetization (caused by either higher temperatures due to insufficient/ineffective thermal management and/or faulty conditions) [6]. Flux-switching permanent magnet (FSPM) machines are regarded as a promising candidate. They have high torque density due to the flux-concentration effect and the location of PMs on the stator makes them more favorable for thermal management. In addition, the passive rotor is mechanically simple and robust as in the case of SRMs [7], [8].

Many design variants of FSPM machines have been investigated. For example, compared with the conventional double-layer winding, FSPM machines with the same stator/rotor pole combinations, the flux linkage and back-electromotive force (EMF) of machines with single-layer winding are more likely to be asymmetrical, which can have significant impact on losses and torque ripple [9]. A C-core 6/13

stator/rotor pole FSPM machine with very large slot opening exhibits 40% larger back-EMF and average torque than those of the conventional 12/10-pole machine, but both the magnetic and electric loadings of the two motors are different [10]. A modular topology of a FSPM machine was proposed in reference [11], in which, the PMs in alternate stator pole are removed. Due to the better magnetic isolation, the self-inductance increases while the mutual inductance decreases, which improves the fault-tolerance capability. A novel E-core hybrid-excitation FSPM machine was designed and optimized in [12], the mutual inductance of the two adjacent phases is significantly reduced due to the magnetic isolation caused by the fault-tolerant teeth of the E-core. On the other hand, the field-excited winding wound around the fault-tolerant teeth improves the flux-weakening capability. An outer-rotor FSPM machine with wedge-shaped magnets is presented in [13]. Compared with the rectangular-shaped magnets machine, its average torque and efficiency have been increased. Even though there is a lot of work done in this space, there is still a need for more comprehensive, quantitative, “apples-to-apples” comparison of various FSPM topologies. Moreover, most of the references were focused on three-phase machines. It has been shown in the literature that for various machine topologies, the multi-phase machines (greater than 3) have advantages in terms of fault-tolerance, reduced torque ripple, and improved control capabilities [14]–[15][16]. Thus, a comprehensive quantitative comparison and analysis of multi-phase FSPM machines will be a valuable addition to the body of work that already exists in the literature.

Large-scale design optimization techniques have been a well-established practice to obtain better performance in electric machines. Such optimization techniques include two key segments: 1) An accurate computation model to evaluate the electromagnetic performance subjected to variations in various design parameters. 2) An optimization algorithm to search for the globally optimal solution [17]. In terms of the computation model, the recently developed computationally efficient finite-element analysis (CE-FEA) offers an effective solution for high-fidelity and fast simulation of three-phase PMSMs [18], [19]. It is very suitable for optimization, particularly large-scale optimization process, due to the fact that the computational burden is significantly reduced in CE-FEA compared with the conventional time-stepping FEA (TS-FEA) simulation. However, the present CE-FEA method will be invalid when the electromagnetic information is asymmetrical. Reference [9] and [20] analyzed the conditions to obtain symmetrical phase back-EMF waveforms for FSPM machines. It means that for certain stator/rotor pole combinations, there are even harmonic components in the back-EMF waveforms, *i.e.*, the waveforms are asymmetrical. Thus, it is imperative to expand the application scope of the CE-FEA method so that it can cope with machines with even harmonic components.

On the other hand, some optimized FSPM designs have been presented in literature. Reference [21] analyzed the influence of rotor pole-arc on the performance of a 12/10-pole FSPM machine. The results show that the optimal rotor pole-arc not only minimized the harmonic components in the phase back-EMF waveforms, but also reduced the cogging torque as well as increased the average torque. In [22], a double mechanical port FSPM machine was optimized to realize the multi-objectives of high torque density, low torque ripple, and low magnetic coupling. In order to improve the optimization efficiency, a response surface methodology and a genetic algorithm were applied. In [23], the sequential subspace optimization method was used to obtain the best performance of a 6/7-pole FSPM machine. The control system was included to have optimum performance of the entire motor-drive system. However, in the previous optimization studies for FSPM

machines, largely the electromagnetic performance at rated operating point was taken into consideration, while the performance in the high-speed region was largely ignored.

In this paper, these authors will provide a comprehensive comparison of multi-phase PMSM machines with different topologies. The comparison will include the electromagnetic performance in the low-speed region, the flux-weakening performance/capability in the high-speed region, as well as the fault-tolerance capability under faulty conditions. Moreover, in order to reduce the computational burden during the large-scale optimization process, the CE-FEA is expanded for both multi-phase motors and asymmetrical conditions. Furthermore, a multi-objective optimization is implemented, in which the performance of the motor in both the low- and high-speed regions are taken into account.

SECTION II. Performance Comparison of Five-Phase FSPM Machines With Different Topologies

Four typical outer-rotor five-phase FSPM machines are designed and compared in this section. These include a double- layer winding, a single-layer winding, a C-core, and an E-core types, as shown in Fig. 1. The double-layer winding topology is the conventional topology in which a nonoverlapping coil is wound around each stator pole. By contrast, the single-layer winding design uses alternate poles wound windings. Compared to the C-core motor, an auxiliary fault-tolerant tooth is added to each stator core in the E-core motor. Their main ratings and design parameters are listed in Table I. It should be noted that the rotor geometry, the total slot area, and the PM cross-sectional area of the four motors are the same. In addition, the stator/rotor pole combinations are chosen because these combinations provide a relatively high winding factor [24].

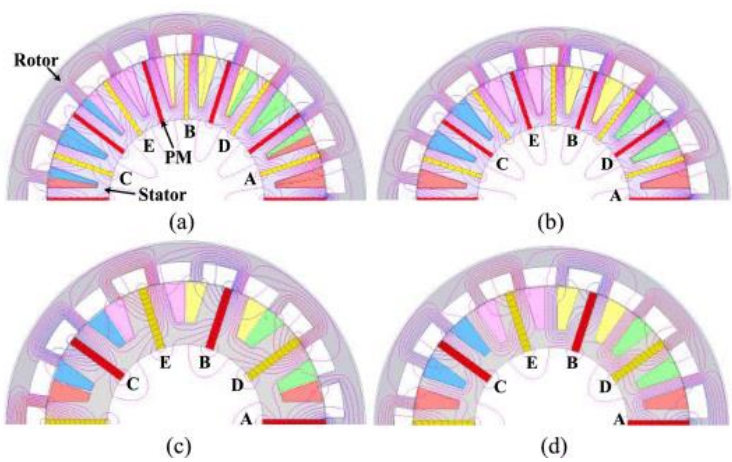

Fig. 1. Cross-sections of the investigated five-phase FSPM machines. (a) Double-layer winding. (b) Single-layer Winding. (c) C-core. (d) E-core.

TABLE I Parameters of the Four Investigated Machines

Parameter Value	Parameter	Value
Supply voltage (VDC) 110	Rotor outer radius (mm)	112.5
Rated phase current (A) 10	Rotor inner radius (mm)	88.5
Rated speed (r/min) 200	Air-gap length (mm)	0.5
Number of phases 5	Stator inner radius (mm)	49
Stator pole number 20/20/10/10	Stack length (mm)	85

Rotor pole number 21	Number of turns/phase	92
Winding factor 0.98/0.99/0.95/0.95	**PM** remanence NdFeB (T)	1.23

A. Electromagnetic Performance in the Low-Speed Region

The air-gap flux density profiles of the four motors under open-circuit condition, while the rotors are aligned along the *d*-axis are depicted in Fig. 2. It can be seen that the flux density profiles of double-layer winding and single-layer winding motors are identical due to the fact that there is no difference between the two motors under open-circuit condition. In addition, the air-gap flux density profiles of all case-studies are non-sinusoidal, and the peak values are as high as 2T because of the flux-concentration effect. The back-EMF waveforms at the speed of 200 r/min and their corresponding harmonic order components are shown in Fig. 3. This figure indicates that the back-EMF waveforms of the four topologies are symmetrical without even harmonic components. The fundamental component of the E-core motor is the highest while that of the double-layer winding motor is the lowest, although the four motors have the same number of rotor poles and number of turns per phase.

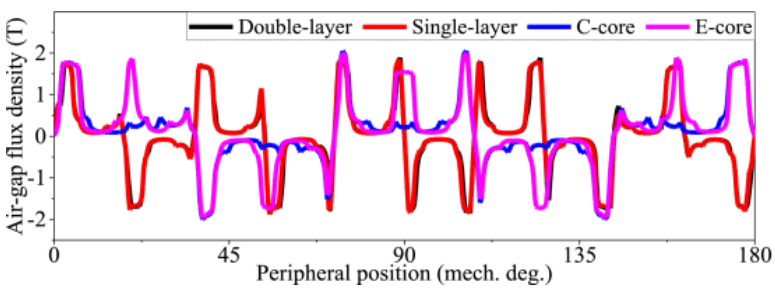

Fig. 2. Radial air-gap flux density.

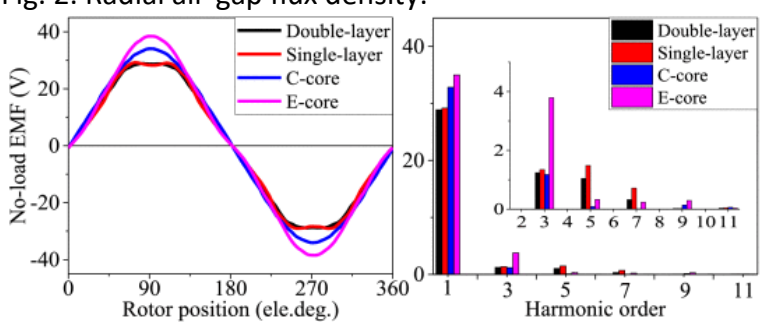

Fig. 3. Back-EMF and harmonic components.

In the low-speed region, motors for traction applications typically need to produce sufficient constant average torque T_{avg} to provide enough acceleration and hill-climbing capabilities. Other requirements include: low cogging torque, T_{cog}, low torque ripple, T_{ripple}, and low total harmonic distortion (*THD*) of the back-EMF to limit vibrations and acoustic noise, high power factor, P_f, to improve the utilization of power converters, high efficiency for energy savings. These performance parameters of the four motors are summarized in Table II, where n_b is the corner/base speed at rated voltage and current, ψ_m is the PM flux linkage, and L_d is the *d*-axis inductance. It can be seen that the double-layer winding motor has the lowest PM flux linkage and average torque, highest power factor and efficiency. The cogging torque of the double-layer winding and single-layer winding motors are the lowest. Compared to the conventional double-layer winding motor, the single-layer winding motor has higher

PM flux linkage and average torque. The C-core motor has the lowest *THD*, torque ripple, and power factor. By contrast, the PM flux linkage and average torque of the E-core motor are the largest, even though its cogging torque is the highest and efficiency is the lowest. It is interesting to note that by reducing the number of stator poles, from 20 (double-layer winding motor and single-layer winding motor) to 10 (C-core motor and E-core motor), the PM flux linkage and average torque increased, although the winding factor is reduced from 0.98/0.99 to 0.95/0.95. This means that the C-core and E-core FSPM machines make better use of the available PMs.

TABLE II Performance Parameters of the Four FSPM Machines

	Double-layer	Single-layer	C-core	E-core
N_b(r/ min)	255	248	208	200
$\psi_m(Wb)$	0.0462	0.0467	0.0525	0.0559
$THD(\%)$	5.72	7.29	3.63	10.94
T_{cog}(Nm)	0.12	0.12	0.47	0.79
T_{avg}(Nm)	48.16	48.49	55.12	57.91
$T_{ripple}(\%)$	3.26	4.07	2.72	4.00
P_f	0.94	0.92	0.87	0.89
L_d(mH)	1.99	2.46	3.04	3.33
η(%)	92.50	92.13	92.36	92.02

The torque versus current profiles of the four motors are shown in Fig. 4. These profiles will help estimate the overload capability of the various designs. It is clear that the double-layer winding motor shows the best overload capability while the C-core and E-core motors suffer significantly from magnetic saturation above 2 *pu* current. The reason is that the number of turns per coil of the other three motors are twice that of the double-layer winding motor. This leads to higher armature reaction flux (on local basis) and therefore they become more deeply saturated at higher current for the same number of turns per phase.

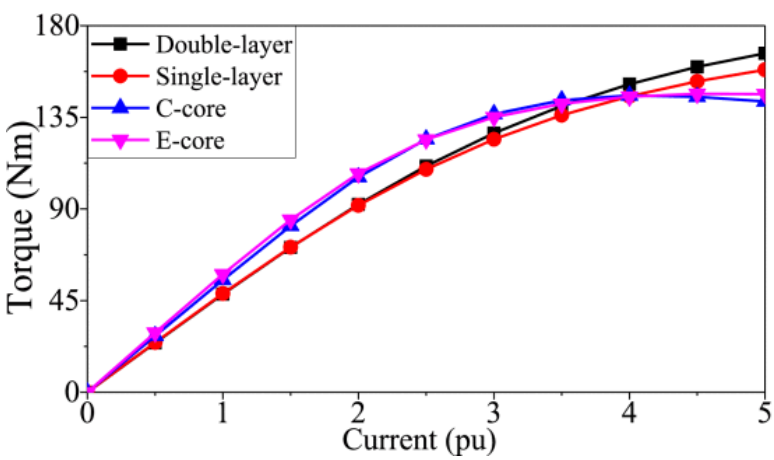

Fig. 4. Variation of torque with current for the four topologies.

B. Flux-Weakening Capability in the High-Speed Region

The flux-weakening capability is particularly important for motors in traction applications since it determines loading capability and speed range in the high-speed region. In principle, the motor is operated in the maximum torque-per-ampere (MTPA) control mode below the corner/base speed. While it is operated in the flux-weakening control mode above the base speed to achieve wider constant power-speed range (CPSR). The input current and voltage are limited by eq. (1) and eq. (2) below, where i_d, i_q, L_d, and L_q are the *d*- and *q*-axis currents and inductances, respectively, i_{lim} and V_{lim} are the current and voltage limits, ω is the angular speed in electrical rad/sec. Thus, the motor operates at the intersection of the voltage limit ellipse and the current limit circle as shown in Fig. 5. The characteristic current, I_{ch}, is defined by eq. (3). Substituting (3) into (2), the voltage equation is expressed by eq. (4). As can be seen, the smaller is the current difference between the characteristic current, I_{ch}, and the rated current, I_{rated}, the wider the CPSR could be [25], [26]. The flux-weakening capability can be evaluated by the flux-weakening coefficient, k_{fw}, expressed in eq. (5).

$$
\begin{aligned}
& i_d^2 + i_q^2 \le i_{lim}^2 \\
& (\omega L_d i_d + \omega \psi_m)^2 + (\omega L_q i_q)^2 \le V_{lim}^2 \\
& I_{ch} = \psi_m / L_d \qquad\qquad (1)(2)(3)(4)(5) \\
& (i_d + I_{ch})^2 + (L_q i_q / L_d)^2 \le [V_{lim}/(\omega L_d)]^2 \\
& k_{fw} = \psi_m / (\psi_m - L_d I_{rated})
\end{aligned}
$$

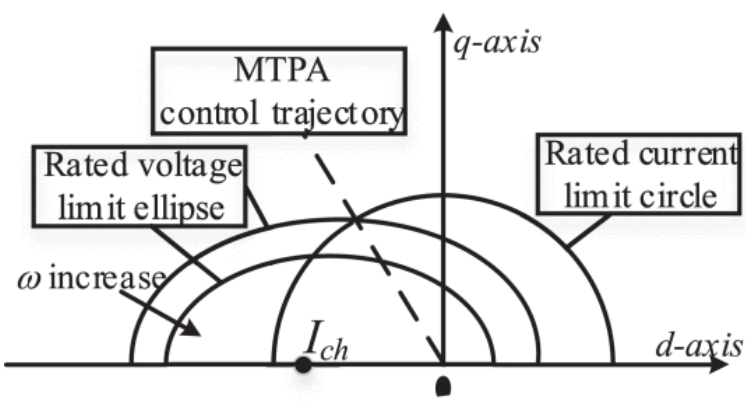

Fig. 5. Field-weakening control trajectory.

The flux-weakening performance of the four motors including torque and power versus speed under current and voltage limits are shown in Fig. 6. This figure indicates that the E-core motor exhibits the best flux-weakening capability, while that of the double-layer winding motor is the weakest. This is due to the fact that the C-core and E-core motors have relatively high *d*-axis inductance than the other two as listed above in Table II.

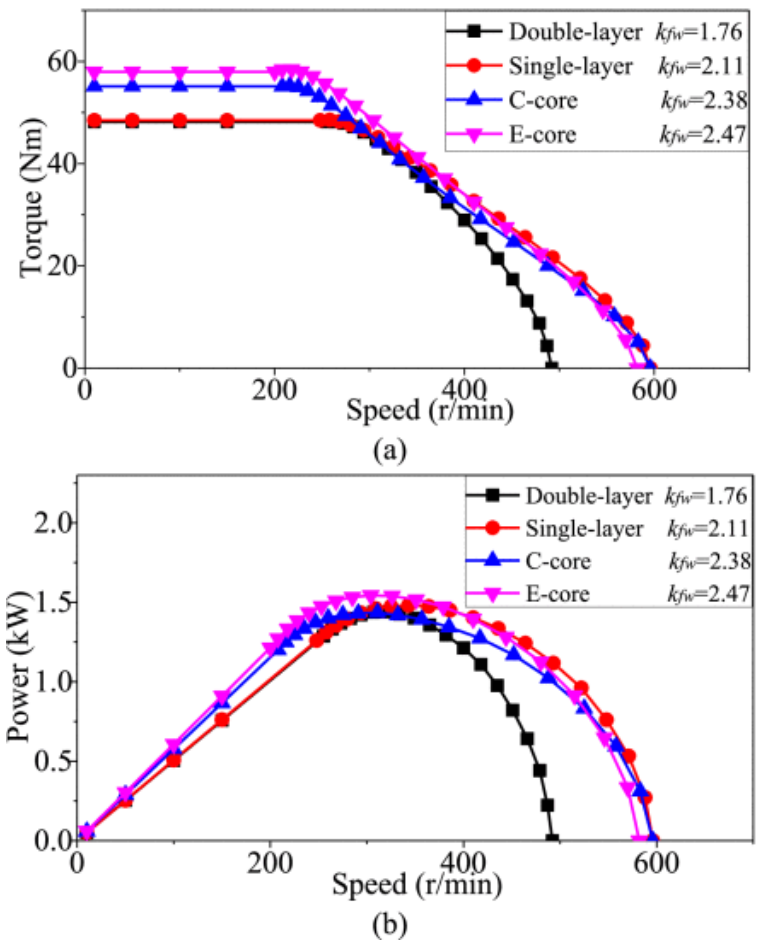

Fig. 6. Flux-weakening capability of the four motors. (a) Torque vs. speed. (b) Power vs. speed.

C. Fault-Tolerance Capability

Fault-tolerance capability is crucial to continue the operation of such a motor-drive under faulty conditions. High self-inductance can effectively limit the short-circuit current while low mutual inductance leads to better magnetic isolation between the various phases. Compared to the conventional double-layer winding motor, the isolated coils of the single-layer winding are expected to reduce the magnetic coupling between phases. Similarly, the middle-tooth of the E-core increases the potential of the physical and magnetic isolation between phases compared to the C-core. Table III compares the self- and mutual inductances of the four motors. It can be seen that the self-inductance of the conventional double-layer winding motor is the lowest, even though it has little mutual inductance. The single-layer motor has the highest self-inductance and relatively low mutual inductance. Compared to the C-core motor, the E-core motor has higher self-inductance and lower mutual inductance. The short-circuit currents in case of terminal short circuit are presented in Fig. 7. This figure shows that the short-circuit current of the single-layer winding motor is the lowest due to its highest self-inductance.

TABLE III Inductances of the Four FSPM Machines

Inductances(mH)	Double-layer	Single - layer	C-core	E-core
L_{AA}	2.36	3.98	3.68	3.76

L_{AB}	0.01	0.06	0.52	0.25
L_{AC}	0.12	0.38	1.32	0.68
L_{AD}	0.12	0.38	1.32	0.67
L_{AE}	0.01	0.06	0.52	0.25

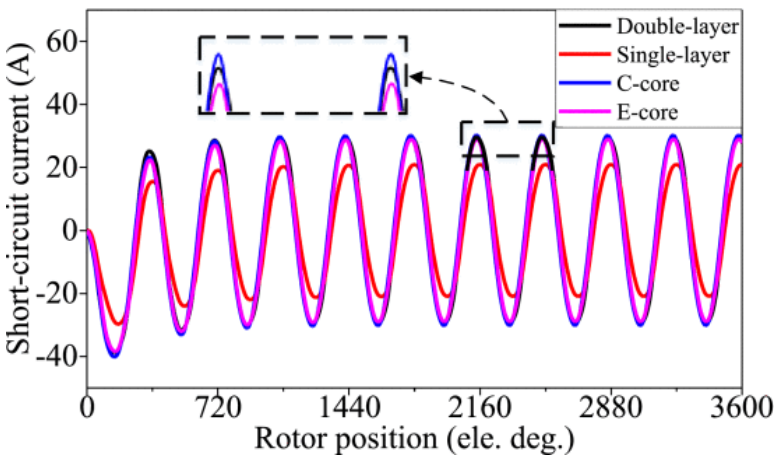

Fig. 7. Short-circuit current.

D. Analysis of Results and Discussion

As mentioned above, the conventional double-layer winding motor has the lowest average torque, flux-weakening capability, and self-inductance, although its power factor, efficiency, and overload capability are the highest. By contrast, the single-layer winding motor has slightly higher average torque, better flux- weakening capability, and the lowest short-circuit current. The average torque and flux-weakening capability of the C-core motor are improved in comparison with the above two motors. The E-core motor has the highest average torque, best flux-weakening capability, and relatively better fault-tolerance capability. Moreover, compared to the C-core motor, the auxiliary fault-tolerant tooth in the E-core motor is helpful to make better use of the PMs and to improve the flux-weakening capability and fault-tolerance capability. Therefore, the E-core motor emerges as the best option in terms of performance and hence is selected to be optimized in the following sections.

According to the conditions for balanced symmetrical back-EMF waveforms in FSPM machines established in [9], it can be concluded that for E-core five-phase FSPM machines with 10 stator poles, the back-EMF waveforms of the motors with odd rotor poles are symmetrical without even harmonic components, but they suffer from unbalanced magnetic force (UMF). On the other hand, those motors with even rotor poles are asymmetrical although there is no UMF. Thus, both design options will be further investigated.

SECTION III. Method to Improve Optimization Efficiency

As previously mentioned, in order to reduce the computational burden, the CE-FEA method is used to evaluate the electromagnetic performance. However, the present CE-FEA method was only implemented for three-phase symmetrical conditions [18], [19]. Accordingly, this method is redeveloped here to be applicable for multi-phase (greater than 3) machines, in both the symmetrical

(illustrated by the example of the E-core five-phase 10/21-pole FSPM machine) and the asymmetrical (illustrated by the example of the E-core five-phase 10/22-pole motor) conditions, respectively.

A. CE-FEA in Symmetrical Condition

In principle, for an m-phase PM machine operating under the condition of symmetrical steady-state load, *m* equidistantly spaced samples of the back-EMF are obtained from a single magnetostatic FE solution, based on the electric circuit symmetry [27]. In addition, based on the half-wave symmetry, the number of points achieved per solution is doubled. In the case of the five-phase motors, this symmetry is expressed by eq. (6), which means that $n \times m \times 2$ points can be reconstructed by *n* magnetostatic FE solutions. The magnetostatic FE solution is implemented by ANSYS/MAXWELL software, while the reconstruction is implemented by post-processing in MATLAB software. As well known, the FE solution in ANSYS/MAXWELL is much more time-consuming than the post-processing in MATLAB. Therefore, compared with the conventional time-stepping FEA (TS-FEA) simulation, the CE-FEA method is much more computationally efficient.

The reconstruction process of the back-EMF waveform and torque profile for an E-core 10/21-pole FSPM machine are shown in Fig. 8 and Fig. 9, respectively. As can be seen in Fig. 8, there are 6 samples in each phase which are calculated using FE solutions in a region spreading over 36°e. Hence, there are 30 samples in half a cycle of 180°e which are obtained using eq. (6). Finally, the points in the region of 180°–360°e are obtained through the concept of half-wave symmetry. As a result, 60 back-EMF data points are available from only 6 magnetostatic FE solutions, which indicates that the computational burden is significantly reduced by up to an order of magnitude. Moreover, the results show satisfactory agreement between the CE-FEA and TS-FEA computed results. Moreover, based on the Nyquist criterion/theorem, the maximum harmonic order, nM, that can be rigorously obtained in Fourier analysis is expressed in eq. (7). This indicates that compared with the three-phase motors, the CE-FEA method is more efficient in machines with higher numbers than three phases.

$$\left.\begin{aligned} e_a(\theta) &= e_a(\theta) \\ e_a(\theta + 36^\circ) &= -e_c(\theta) \\ e_a(\theta + 2 \times 36^\circ) &= e_e(\theta) \\ e_a(\theta + 3 \times 36^\circ) &= -e_b(\theta) \\ e_a(\theta + 4 \times 36^\circ) &= e_d(\theta) \end{aligned}\right\} \quad (6)(7)$$

$$n_M = m \times n - 1$$

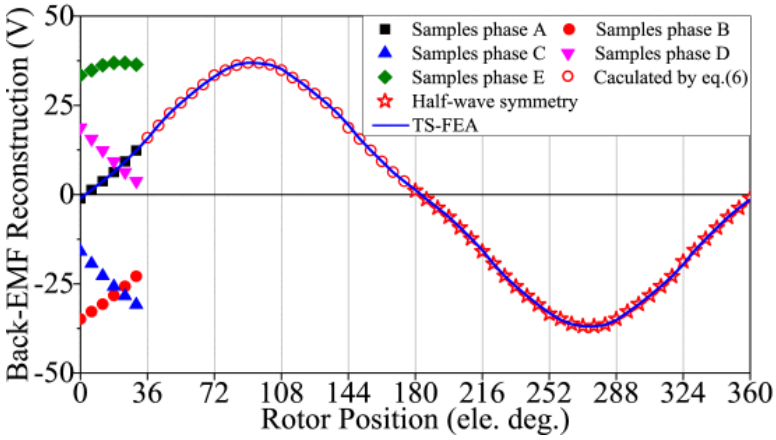

Fig. 8. Reconstruction procedure of back-EMF waveform by 6 FE solutions for the 10/21-p FSPM machine at the rated speed of 200 r/min.

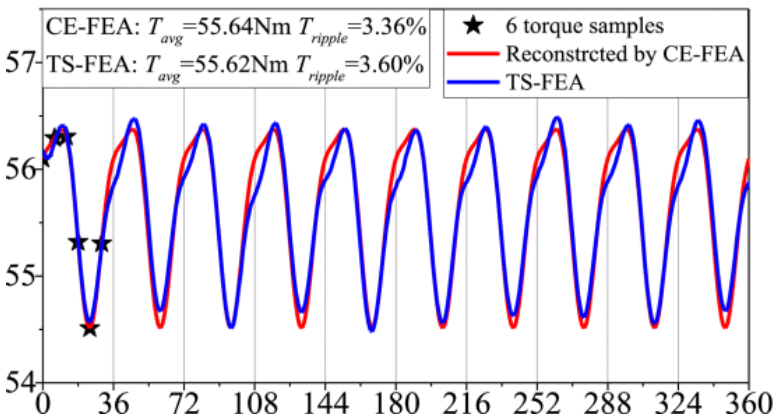

Fig. 9. Reconstructed torque profile of the 10/21-p motor by CE-FEA with the rated current excitation (10 A).

B. Condition CE-FEA in Asymmetrical Condition

In the asymmetrical condition, the method based on half-wave symmetry is invalid due to the even harmonic components present in the back-EMF waveforms. However, the electric circuit is still symmetrical for different phases, e.g., for the E-core five-phase 10/22-pole FSPM machine, it is governed by eq. (8). Differing from that in Part *A* above, *n* magnetostatic FE solutions reconstruct $n \times m$ points at most.

$$\left.\begin{aligned} e_a(\theta) &= e_a(\theta) \\ e_a(\theta + 72°) &= e_e(\theta) \\ e_a(\theta + 2 \times 72°) &= e_d(\theta) \\ e_a(\theta + 3 \times 72°) &= e_c(\theta) \\ e_a(\theta + 4 \times 72°) &= e_b(\theta) \end{aligned}\right\} \quad (8)$$

As shown in Fig. 10, there are 12 magnetostatic FE solutions which are needed in a region spreading over 72°e, which yield 60 points covering the entire electric cycle of 360°e using eq. (8). Similarly, the torque profile is shown in Fig. 11. The TS-FEA results verified the CE-FEA process. By contrast, the maximum harmonic order resulting from Fourier analysis is governed by eq. (9).

$n_M = m \times n/2 - 1$ (9)

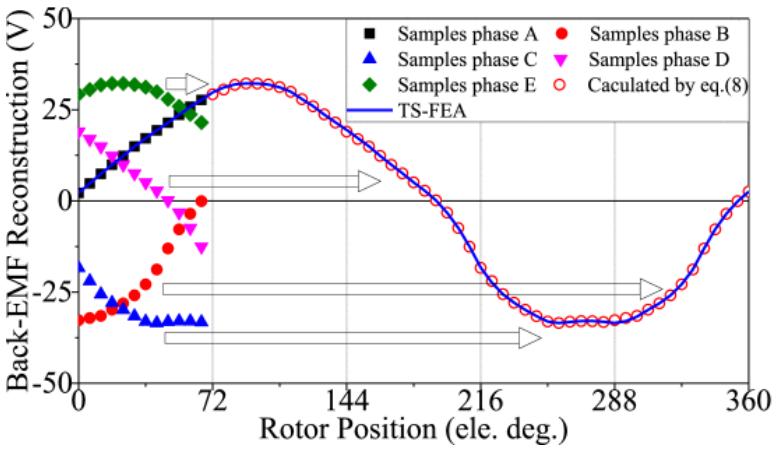

Fig. 10. Reconstruction of back-EMF waveform by 12 FE solutions for the 10/22-p FSPM machine at the rated speed of 200 r/min.

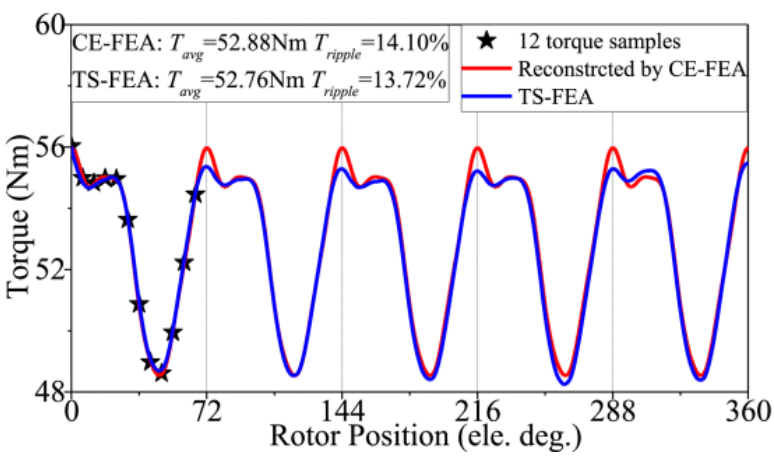

Fig. 11. Reconstructed torque profile of the 10/22-p motor by CE-FEA with the rated current excitation (10 A).

SECTION IV. Optimization

As previously discussed, most of the previous design optimization efforts of FSPM machines that exists in literature largely focused on the low-speed constant-torque region. This will be addressed in this section. A large-scale automated optimization method that takes both the constant-torque and constant-power speed range into consideration is implemented for the two case-studies of the E-core FSPM machines with 10/21-p and 10/22-p combinations, respectively. To reduce the computational burden, the redeveloped CE-FEA method described in Section III above is utilized to estimate the electro-magnetic performance, in conjunction with the DE algorithm is implemented to search for the globally optimal solution.

A. Condition CE-FEA in Asymmetrical Condition

A robust parametric model is developed for the two motors, as shown in Fig. 12. To give a generic point of view and avoid geometrical conflicts during the optimization procedure, the variables are defined by ratio expressions as listed in Table IV, where, R_{ri}, R_{ro}, R_{si}, R_{so} are the inner and outer radii of the rotor and stator, respectively, h_g is the air gap height, β_t is the rotor pole-arc width in degrees, β_b is the rotor tooth-arc width at the yoke, h_r is the rotor tooth height, α_{pm} is the PM arc width, l_{pm} is the PM length, α_t and α_f are the stator tooth and fault-tolerant tooth-arc width, h_{sy} is the stator yoke height. τ_s and τ_r are the stator and rotor pole pitches ($\tau_s = 360°/10$; $\tau_r = 360°/21$, for 21-p motor or 360°/22 for 22-p motor).

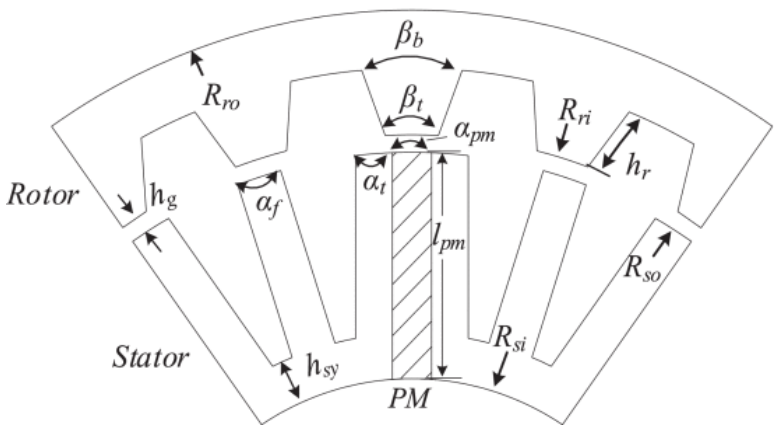

Fig. 12. Parametric model for the two E-core FSPM machines.

TABLE IV Deign Variables and Their Bounds

Var.	Definition	Min	Max	Var.	Definition	Min	Max
k_{si}	R_{ri}/R_{ro}	0.7	0.85	k_{pm}	α_{pm}/τ_s	0.05	0.15
h_g	Fig. 12	0.5	1.2	k_{lpm}	l_{pm}/R_{so}	0.3	0.6
k_r	β_t/τ_r	0.15	0.5	k_{st}	α_t/τ_s	0.1	0.2
k_{ry}	β_b/τ_r	0.15	0.8	k_{ft}	α_f/τ_s	0.1	0.2
k_{hr}	$h_r/(R_{ro} - R_{ri})$	0.3	0.7	k_{sy}	$h_{sy}/(R_{so} - R_{si})$	0.16	0.4

B. Design Specification for DE Algorithm

As a metaheuristic search algorithm, DE has outperformed other stochastic optimizers in electric machine design [28]. Furthermore, the optimal flux-weakening capability occurs when the rated current, I_{rated}, is equal to the characteristic current I_{ch}. It is interesting to note that motors with very low (close to zero) current difference, also possess a good fault-tolerance capability to limit the steady-state terminal short-circuit current to the rated current, due to the one per-unit value of phase inductance (effectively the machine characteristic current is equivalent to the symmetrical multi-phase short-circuit current at the machine terminals) [29], [30]. Therefore, three objectives are given as follows in order to:

- Maximize the torque density by minimizing the stack length;
- Maximize the efficiency given by the expression below:

$\eta = [P_{out}/(P_{out} + P_{Cu} + P_{eddy} + P_{Fe} + P_{fw})] \times 100\%$ (10)

where, P_{out} is the output power, P_{Cu}, P_{eddy}, P_{Fe}, P_{fw} are the losses of copper, eddy-current in PMs, iron core of stator and rotor, as well as friction and windage, respectively. It should be noted that P_{Cu} is calculated according to eq. (11). P_{eddy} and P_{Fe} are calculated using the PM loss and core loss models in ref. [18] and [19]. The mechanical loss is estimated based on previous experience with the 1kW prototype PM machine in ref. [31].

$P_{Cu} = mI^2R_{ph}$ (11)

where, *m* is the number of phases, *I* is the root-mean-square phase current, R_{ph} is the phase resistance. Due to the machine low speed/frequency, AC copper losses are not significant.

- Maximize the flux-weakening capability and the fault-tolerance capability in the event of terminal short circuit by minimizing the current difference, I_{dif}, between the rated and characteristic currents:

$I_{dif} = |(I_{rated} - I_{ch})/I_{rated}||$ (12)

Meanwhile, two constraints are defined as:

- Total harmonic distortion (*THD*) of the back-EMF, ≤ 20%;
- Torque ripple at the rated load condition, $T_{ripple} \leq 5\%$..

The optimization process is depicted in Fig. 13. There are three main steps in the DE algorithm [32]:

1. Initialization. The first-generation population is randomly initialized using predefined variable ranges such as those in Table IV above. Their performance metrics are evaluated using the CE-FEA method.
2. Crossover and mutation. The new trial vector, ui, is updated by adding the weighted difference between two population vectors to a third vector based on the crossover and mutation ideas as follows:

$$u_i \begin{cases} x_{r0} + F(x_{r1} - x_{r2}), & \text{if } [\text{rand}(0,1) \leq C_r] \\ x_i, & \text{otherwise.} \end{cases} \quad (13)$$

where, x_{r0}, x_{r1}, x_{r2} are three randomly selected present population members, F is the positive real difference scale factor, C_r is the predefined crossover probability, x_i is the parameter of the present population member.

1. Selection. The trial vector, u_i, will replace the present member, x, to enter the next generation, only if its objective function, $f(u)$, is better than that of the present member, $f(x)$.

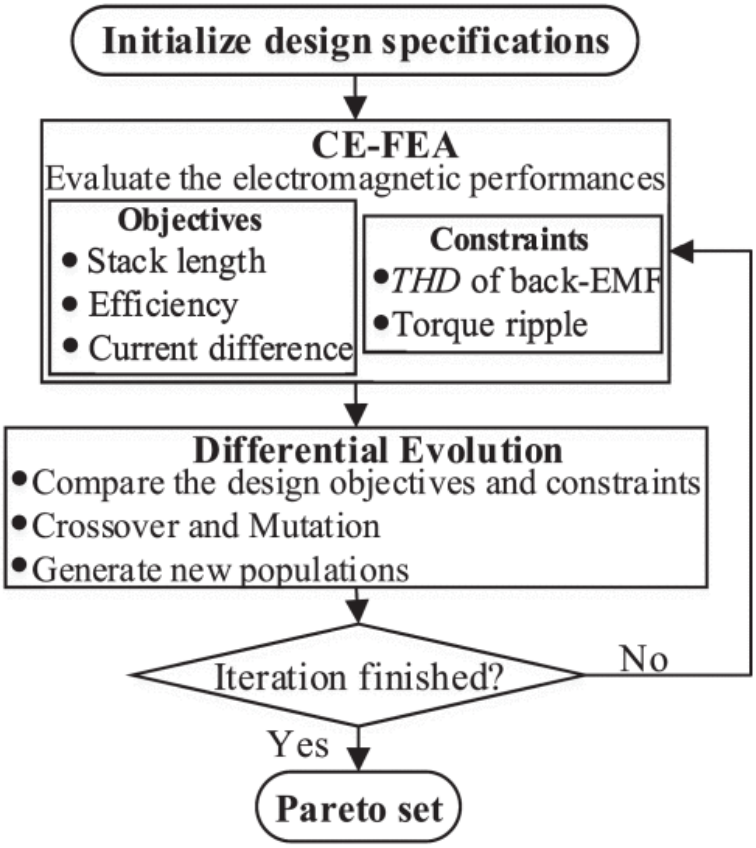

Fig. 13. Flowchart of the automated optimization process.

During the process, the outer diameter of each candidate is fixed while the stack length is scaled to achieve the desired torque output rating of 60 Nm output torque at 200 r/min.

C. Analysis of Optimization Results

The DE algorithm generated 20,000 candidates with 200 iterations and 100 designs per generation. The optimization results of the two motors are shown in Fig. 14. It can be seen that as expected, conflicts exist between the three objectives. The optimal designs are located within the black circle. Comparison of the Pareto-optimal set of these objectives for the two motors are performed in Fig. 15 and Fig. 16, respectively. It can be seen that as the iterations increase, the candidates converge to the Pareto front. Moreover, designs with better performance for one objective are also located in the better region for the other objective, which indicates that the DE algorithm works effectively for the fulfilment of multiple objectives.

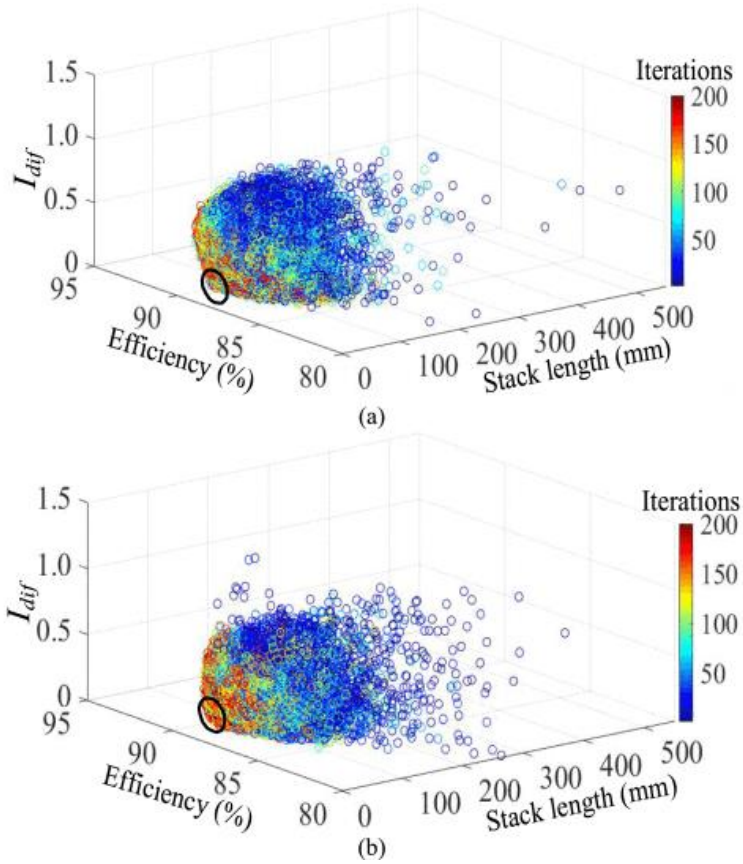

Fig. 14. Optimization results. (a) 10/21-p motor. (b) 10/22-p motor.

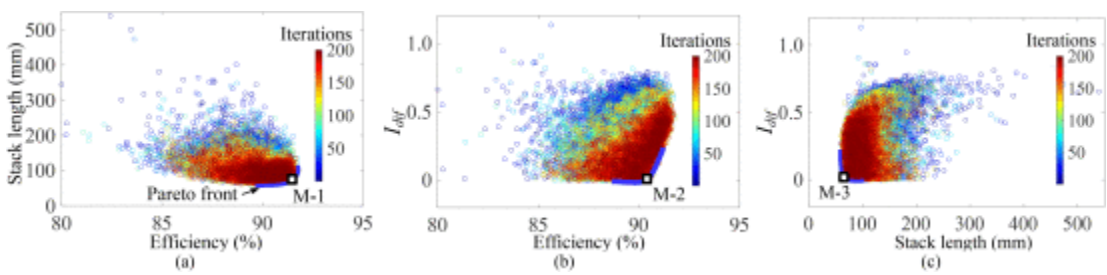

Fig. 15. Pareto sets for DE optimization of 10/21-p motor. (a) Stack length vs. efficiency. (b) Current difference vs. efficiency. (c) Current difference vs. stack length.

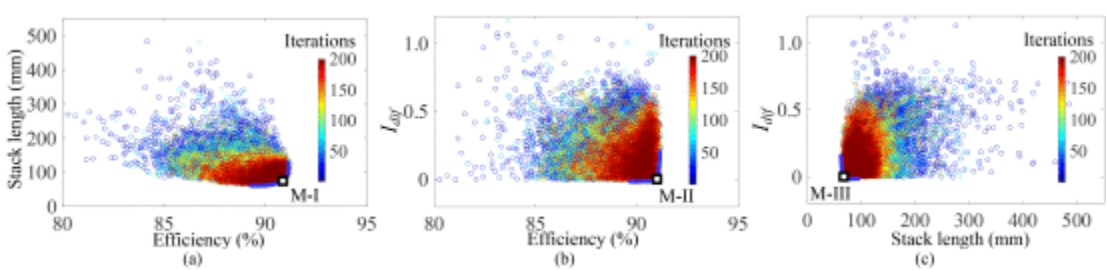

Fig. 16. Pareto sets for DE optimization of 10/22-p motor. (a) Stack length vs. efficiency. (b) Current difference vs. efficiency. (c) Current difference vs. stack length.

It should be noted that there is no unique global best design in multi-objective problems. Instead, a "best compromise" can be obtained based on the Pareto front in engineering practice. Thus, three candidate optimal designs from the Pareto front are selected for 10/21-p and 10/22-p motors, respectively. Their main parameters and performance are listed in Table V.

TABLE V Main Properties of the Optimal Designs

		10/21-p			10/22-p	
	M 1	M 2	M-3	M-I	M-II	M-III
h_g (mm)	0 53	0 82	0.92	0.50	0 78	0.83
R_{si} (mm)	35.47	39.96	38.72	36.17	38.06	36.57
THD (%)	9.38	5.35	5.19	17.31	13.06	17.26
L_d (mH)	3.37	5 83	5.90	3.78	5 56	5 61
Shaft torque (Nm)	60	60	60	60	60	60
T_{ripple} (%)	2.75	1.86	0.95	18.86	22.84	15.02
P_f	0 882	0 702	0.694	0.845	0 709	0 699
Stack length (mm)	72.96	80.12	66.00	70.52	78.62	65.56
η (%)	91.36	90.26	89 38	90.89	90.55	89.82
I_{dif}	0.4296	0.0026	0.001 5	0.3136	0.0045	0.0012

It is interesting to note that the motors with wide CPSR (current difference is close to zero), e.g., M-2, M-3, M-II, and M-III have relatively low power factor. The reason is that the motors with better flux-weakening capability require high inductance which leads to lower power factor mainly at the corner speed. Compared to the 10/21-p motors, the 10/22-p motors have slightly higher torque density, however, their *THD* and torque ripple are significantly higher due to the asymmetrical back-EMF waveforms. Minimizing torque ripple is a typical requirement in high performance applications. Therefore, the 10/21-p motors are preferable.

SECTION V. Prototype and Experimental Validation

Here, design M-3 is selected for prototyping due to the fact that it has almost zero I_{rated} and I_{ch} current difference, and therefore achieves very good flux-weakening capability and fault-tolerance capability in the event of a short-circuit. Also it has a fairly small stack length which indicates good torque density, while still possessing a relatively high efficiency, hence offering a good tradeoff within the three optimization objectives. The prototype is shown in Fig. 17. The specifications of the prototype are listed in Table VI.

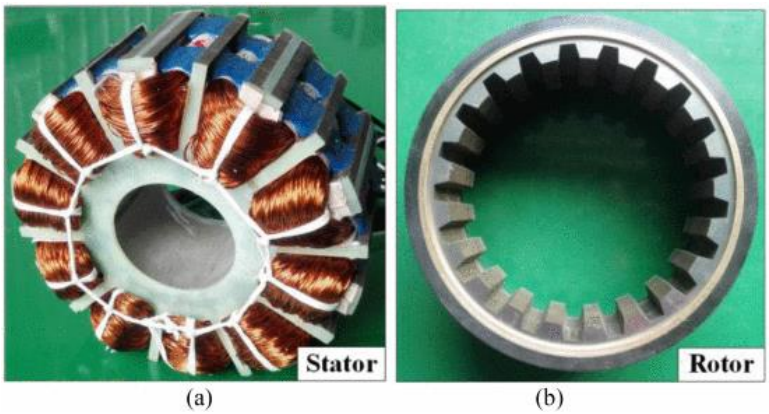

Fig. 17. Prototype of the Five-phase FSPM Machine. (a) Stator. (b) Rotor.

TABLE VI The Specifications of the Prototype

Parameter	Value
Shaft thickness (mm)	13.72
Bearing	2×SKF61907(C=10.8kN, C_0=7.8kN)
Slot insulation	PASU(0.1mm, Class H, 180°C)
Wires	QZY-2/180(Wire diameter: 0.75mm, number of strands:5)
Ferromagnetic sheets	B35A300
Material of PM	NTP300/160(NdFeB, $B_r = 1.23$T, $H_c = 886$KA/m)
Rated phase voltage (V)	40.86
Rated phase current (A)	10
Output Power (kW)	1.26
Phase resistance (ohm)	0.23
P_{Cu} (W)	115.31
P_{Fe} (W)	11.76
P_{eddy} (W)	6.11
P_{fw} (W)	16.09

The flux density distribution plot of the prototyped motor at rated load is shown in Fig. 18. As can be seen, a reasonable level of saturation is maintained in both the stator and rotor teeth. The thermal distribution of the prototyped motor at steady state is shown in Fig. 19, while its transient maximum temperature plot is shown in Fig. 20. The thermal analysis results indicate that the maximum temperature of this motor (about 70 °C) is lower than the limitation of wire insulation, slot insulation, and PM demagnetization, which are 180 °C, 180 °C, and 160 °C (see Table VI), respectively. The finite-element predicted UMF of the prototyped motor at rated load is depicted in Fig. 21. The maximum UMF is about 942N, which is much lower than the basic static loading rating of the bearing (2 × 7.8 kN, see Table VI). Hence, this motor has the capability of long-term safe/stable operation.

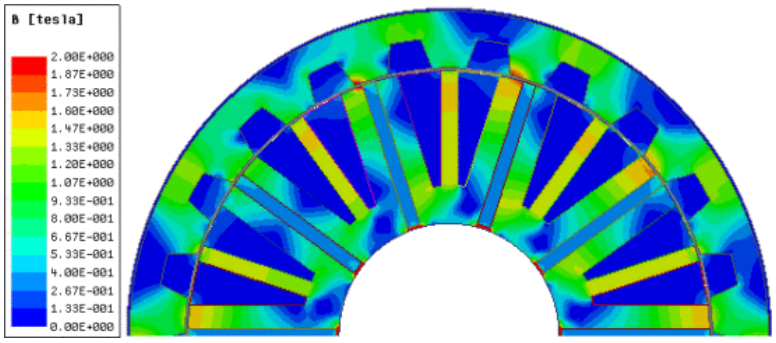

Fig. 18. Flux density distribution plot of the prototyped motor at rated load.

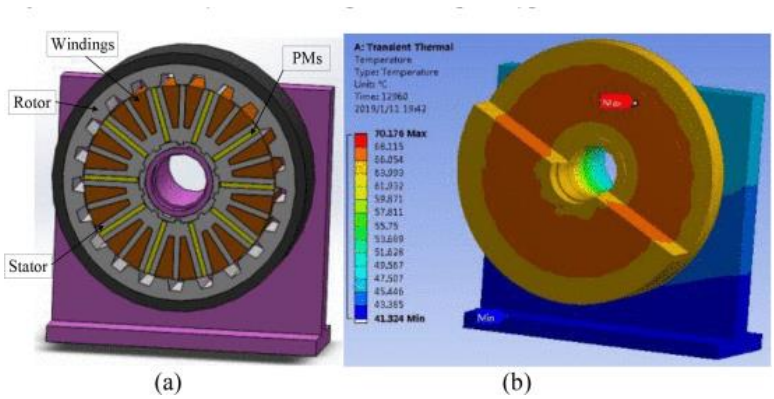

Fig. 19. Thermal distribution of the prototyped motor at rated load. (a) Structure of the prototyped motor. (b) Thermal distribution result.

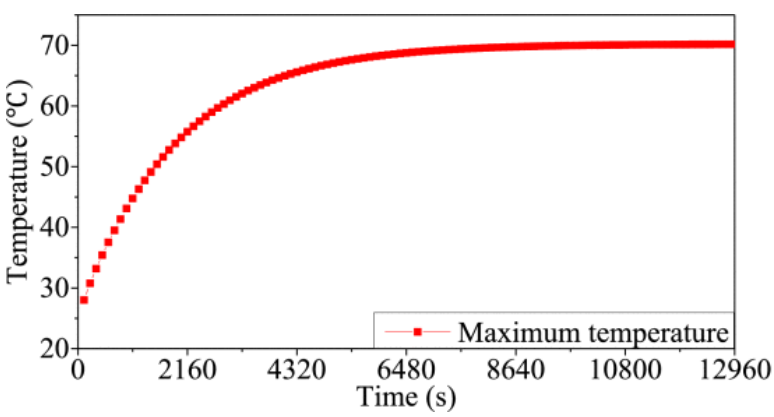

Fig. 20. Transient maximum temperature plot of the prototyped motor at rated load.

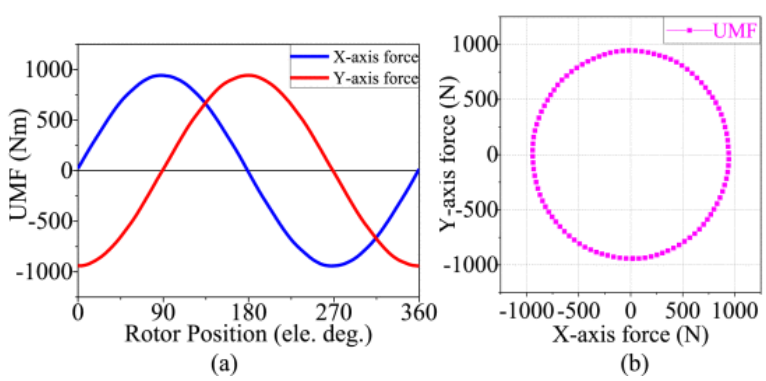

Fig. 21. Finite-element predicted UMF of the prototyped motor. (a) UMF waveforms. (b) Loci of the UMF.

The phase back-EMF validation under open circuit condition at 200 r/min is shown in Fig. 22. The results show that both the CE-FEA and TS-FEA methods have satisfactory accuracy. In addition, it is evident that the motor has fairly sinusoidal and symmetrical back-EMF waveform, which makes it suitable for BLAC operation. This is also clear from the harmonic spectrum of the back-EMF waveform.

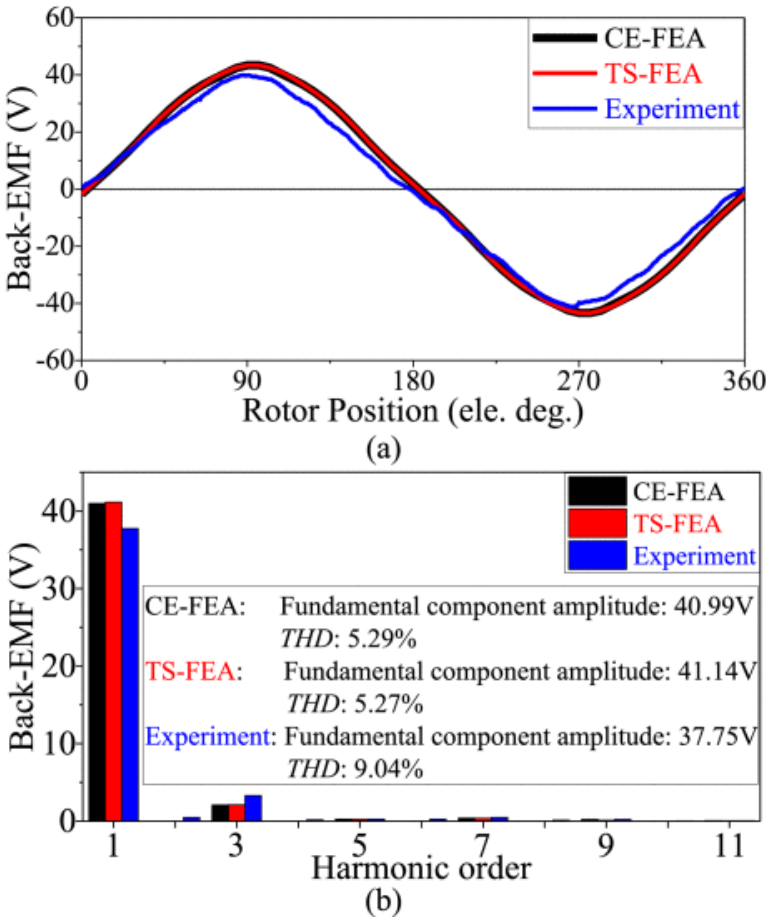

Fig. 22. (a) Predicted and measured back-EMF of the FSPM machine @ 200 r/min. (b) Harmonic spectrum.

The measured and simulated Phase *A* self-inductances are shown in Fig. 23. The average measured value is 8.03 mH, which is 9.6% higher than the TS-FEA prediction. This difference is due to the end winding effect, manufacturing imperfections, and measurement inaccuracy. The frequency of the measured self-inductance is twice the back-EMF frequency, which is consistent with the FEA simulation results.

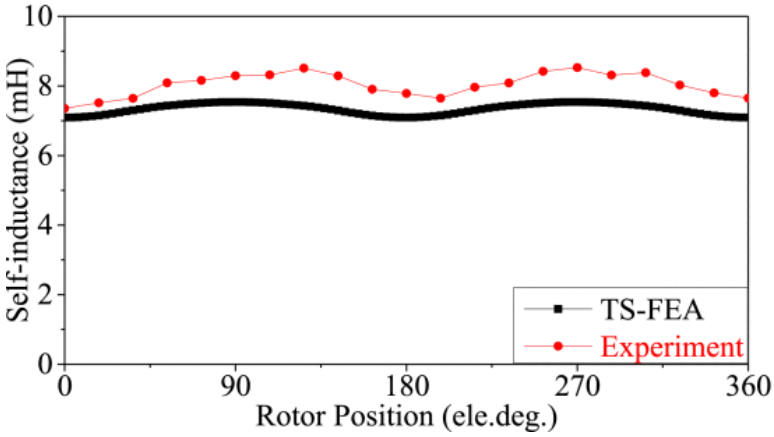

Fig. 23. Measured and FEA predicted Phase *A* self-inductance waveforms of the prototyped motor.

The torque waveforms of the prototyped motor from FEA predictions and experimental measurements are shown in Fig. 24(a) and (b), respectively. It should be noted that the average electromagnetic torque is slightly higher than the rated torque value of 60 Nm, due to the fact that mechanical losses are neglected in the commercial FE simulation software (ANSYS/MAXWELL). More importantly, the torque waveforms from CE-FEA and TS-FEA are in good agreement. In addition, significant signal interference exists in the measured torque waveform [see Fig. 24(b)], which makes the measured torque ripple difficult to identify. Similar phenomena are observed in ref. [33]. This is because the measured torque ripple is composed of cogging torque, PWM switching effects, speed instability, and mechanical friction and vibration. While in the simulated torque waveforms, only the cogging torque predicted from FE simulation is added to the electromagnetic torque. Nevertheless, the average measured torque is in acceptable agreement with the calculated rated torque of 60 Nm, although with a discrepancy of about 11% caused by end-effects, imperfections of manufacturing and assembling process, material properties variations, as well as measurement inaccuracies. Overall, it is fair to state that the experimental results are in satisfactory agreement with the simulation ones.

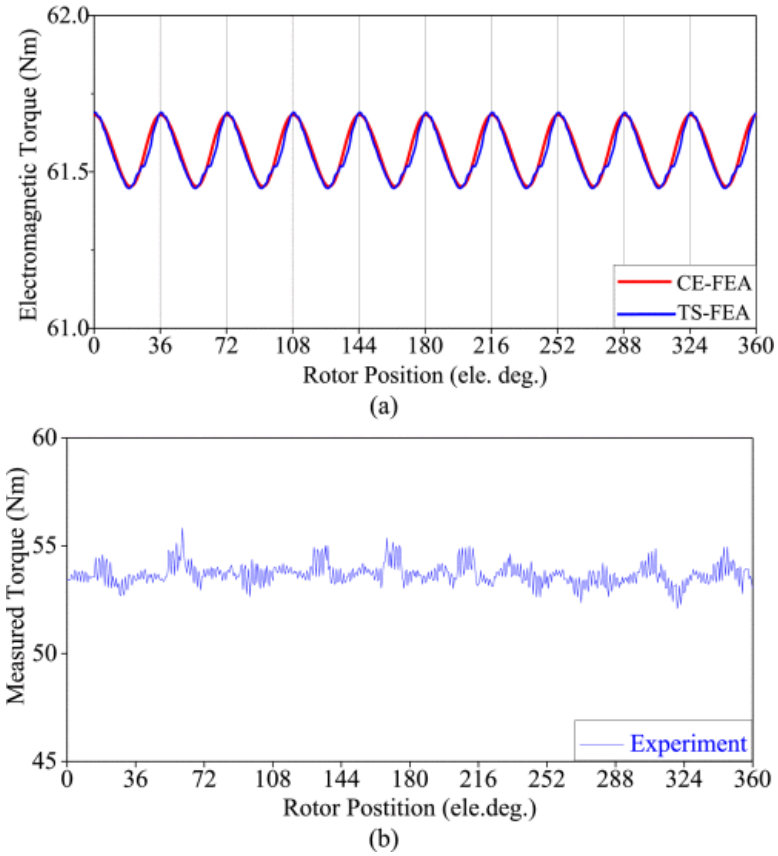

Fig. 24. Torque waveforms of the prototyped motor. (a) Simulated results by CE-FEA and TS-FEA. (b) Measured results.

The torque versus load angle at rated current are depicted in Fig. 25. This figure shows that the measured and model-computed results are also in good agreement. The maximum torque is located near a load angle equal to 90 electrical degrees, which means that the reluctance torque of the FSPM motor is negligible and therefore, $i_d = 0$ control mode is valid for this motor below the base speed. The cogging torque waveform of the prototyped motor predicted by TS-FEA is shown in Fig. 26. The maximum cogging toque is about 0.14 Nm.

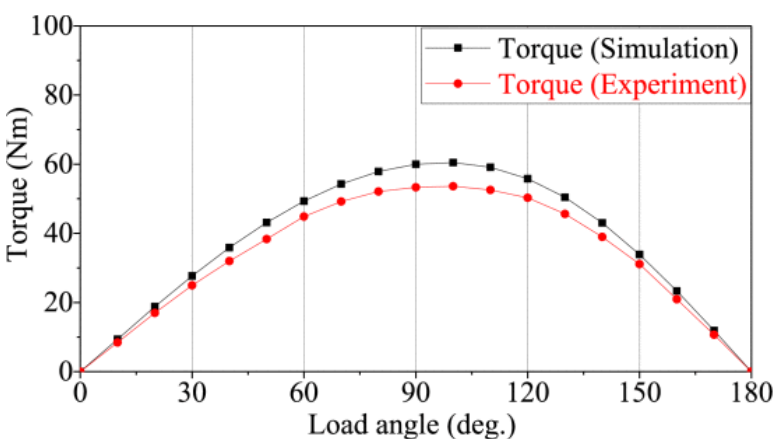

Fig. 25. Torque versus load angle.

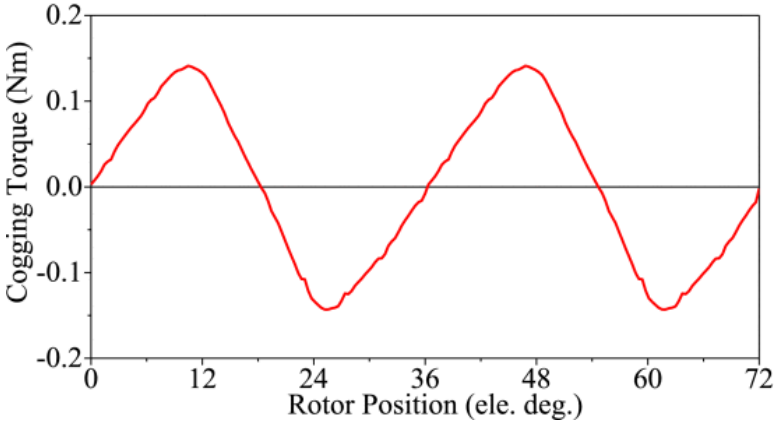

Fig. 26. Cogging torque waveform of the prototyped motor predicted by TS-FEA.

The efficiency and power factor maps of the prototyped motor are shown in Fig. 27(a) and (b), respectively. They are calculated using FEA with 3200 sample operating points equidistantly distributed throughout the torque-speed plane. As can be seen, the extended range of high-efficiency contour is wide, which is of significant importance for the designed motor in traction applications in which the operating points is continuously changing. While the power factor map is a typical one for traction applications.

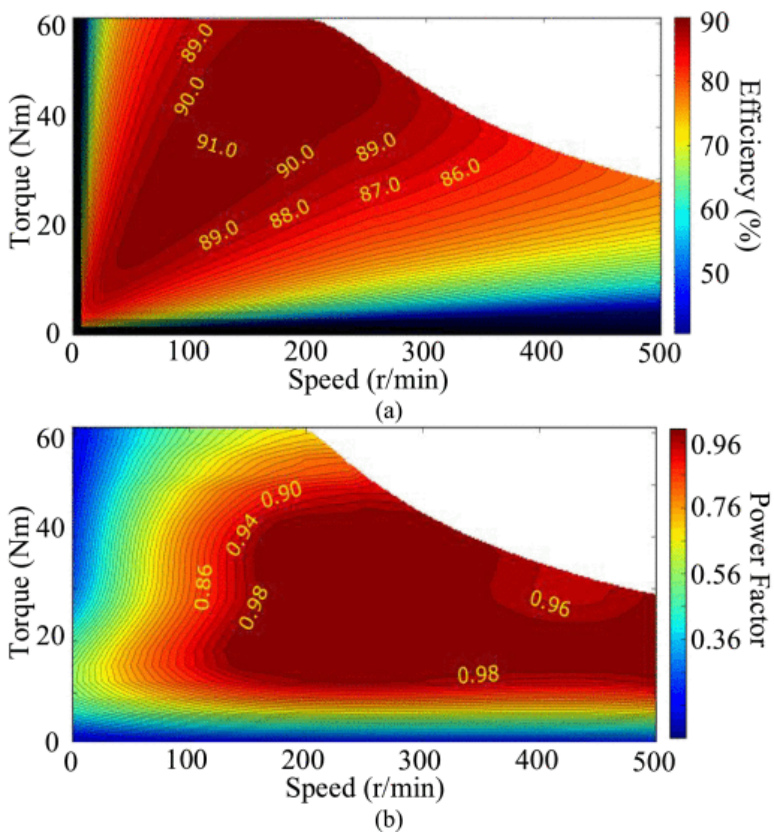

Fig. 27. Efficiency and power factor maps of the prototyped motor. (a) Efficiency map. (b) Power factor map.

SECTION VI. Conclusion

In this paper, four different topologies of five-phase outer-rotor FSPM machines were compared in detail. The comparison included torque characteristics in the low-speed region, flux-weakening capability in the high-speed region, and the fault-tolerance capability. As a result, the E-core motor emerged as the most promising candidate for further comprehensive consideration.

In order to reduce the computational burden, the CE-FEA technique was redeveloped for multi-phase (greater than 3) machines under both the symmetrical and asymmetrical conditions. It is shown that the CE-FEA method is even more effective for these categories of multi-phase motors. When CE-FEA results are compared to results from the TS-FEA method, satisfactory accuracy and significant reduction of execution time are achieved, based on the results provided by two case-studies of FSPM machines with 10/21-p and 10/22-p combinations.

Based on the advantages of the proposed CE-FEA method, a large-scale optimization of the two FSPM machines was implemented using the DE algorithm, in which, the performances in both the low- and high-speed regions were taken into consideration. Consequently, the optimal designs of the E-core 10/21-p and 10/22-p FSPM machines obtained from the Pareto fronts were found superior and hence selected and compared. Accordingly, a design was selected for prototyping. Finally, the prototype and experimental results verified the validity of the proposed analysis process given in this paper.

ACKNOWLEDGMENT

The authors would like to express sincere thanks to ANSYS, Inc. for the software support.

References

1. A. Emadi, Y. J. Lee, K. Rajashekara, "Power electronics and motor drives in electric hybrid electric and plug-in hybrid electric vehicles", *IEEE Trans. Ind. Electron.*, vol. 55, no. 6, pp. 2237-2245, Jun. 2008.

2. Y. Chen, J. Wang, "Energy management and driving strategy for in-wheel motor electric ground vehicles with terrain profile preview", *IEEE Trans. Ind. Inform.*, vol. 10, no. 3, pp. 1938-1947, Aug. 2014.

3. S. U. Chung, S. H. Moon, D. J. Kim, J. M. Kim, "Development of a 20-pole-24-slot SPMSM with consequent pole rotor for in-wheel direct drive", *IEEE Trans. Ind. Electron.*, vol. 63, no. 1, pp. 302-309, Jan. 2016.

4. K. M. Rahman, B. Fahimi, G. Suresh, A. V. Rajarathnam, M. Ehsani, "Advantages of switched reluctance motor applications to EV and HEV: Design and control issues", *IEEE Trans. Ind. Appl.*, vol. 36, no. 1, pp. 111-121, Jan. 2000.

5. A. Haddoun, M. E. H. Benbouzid, D. Diallo, R. Abdessemed, J. Ghouili, K. Srairi, "Modeling analysis and neural network control of an EV electrical differential", *IEEE Trans. Ind. Electron.*, vol. 55, no. 6, pp. 2286-2294, Jun. 2008.

6. Y. Du, C. Zou, X. Zhu, C. Zhang, F. Xiao, "A full-pitched flux-switching permanent-magnet motor", *IEEE Trans. Appl. Supercond.*, vol. 26, no. 4, pp. 1-5, Jun. 2016.

7. Y. Shi, L. Jian, J. Wei, Z. Shao, W. Li, C. C. Chan, "A new perspective on the operating principle of flux-switching permanent-magnet machines", *IEEE Trans. Ind. Electron.*, vol. 63, no. 3, pp. 1425-1437, Mar. 2016.

8. J. D. McFarland, T. M. Jahns, A. M. EL-Refaie, "Analysis of the torque production mechanism for flux-switching permanent-magnet machines", *IEEE Trans. Ind. Appl.*, vol. 51, no. 4, pp. 3041-3049, Jul. 2015.

9. J. T. Chen, Z. Q. Zhu, "Winding configurations and optimal stator and rotor pole combination of flux-switching PM brushless AC machines", *IEEE Trans. Energy Convers.*, vol. 25, no. 2, pp. 293-302, Jun. 2010.

10. J. T. Chen, Z. Q. Zhu, S. Iwasaki, R. P. Deodhar, "Influence of slot opening on optimal stator and rotor pole combination and electromagnetic performance of switched-flux PM brushless AC machines", *IEEE Trans. Ind. Appl.*, vol. 47, no. 4, pp. 1681-1691, Jul. 2011.

11. R. L. Owen, Z. Q. Zhu, A. S. Thomas, G. W. Jewell, D. Howe, "Alternate poles wound flux-switching permanent-magnet brushless AC machines", *IEEE Trans. Ind. Appl.*, vol. 46, no. 2, pp. 790-797, Mar. 2010.

12. W. Hua, P. Su, M. Tong, J. Meng, "Investigation of a five-phase E-core hybrid-excitation flux-switching machine for EV and HEV applications", *IEEE Trans. Ind. Appl.*, vol. 53, no. 1, pp. 124-133, Jan. 2017.

13. W. Hua, H. Zhang, M. Cheng, J. Meng, C. Hou, "An outer-rotor flux-switching permanent-magnet-machine with wedge-shaped magnets for in-wheel light traction", *IEEE Trans. Ind. Electron.*, vol. 64, no. 1, pp. 69-80, Jan. 2017.

14. S. Payami, R. K. Behera, "An improved DTC technique for low-speed operation of a five-phase induction motor", *IEEE Trans. Ind. Electron.*, vol. 64, no. 5, pp. 3513-3523, May 2017.

15. N. K. Nguyen, F. Meinguet, E. Semail, X. Kestelyn, "Fault-Tolerant operation of an open-end winding five-phase PMSM drive with short-circuit inverter fault", *IEEE Trans. Ind. Electron.*, vol. 63, no. 1, pp. 595-605, Jan. 2016.

16. A. M. El-Refaie, "Fault-tolerant permanent magnet machines: A review", *IET Elect. Power Appl.*, vol. 5, no. 1, pp. 59-74, Jan. 2011.

17. A. Fatemi, D. M. Ionel, N. A. O. Demerdash, T. W. Nehl, "Fast multi-objective CMODE-type optimization of PM machines using multicore desktop computers", *IEEE Trans. Ind. Appl.*, vol. 52, no. 4, pp. 2941-2950, Jul. 2016.

18. G. Y. Sizov, D. M. Ionel, N. A. O. Demerdash, "Modeling and parametric design of permanent-magnet AC machines using computationally efficient finite-element analysis", *IEEE Trans. Ind. Electron.*, vol. 59, no. 6, pp. 2403-2413, Jun. 2012.

19. P. Zhang, G. Y. Sizov, J. He, D. M. Ionel, N. A. O. Demerdash, "Calculation of magnet losses in concentrated-winding permanent-magnet synchronous machines using a computationally efficient finite-element method", *IEEE Trans. Ind. Appl.*, vol. 49, no. 6, pp. 2524-2532, Nov. 2013.

20. D. Li, R. Qu, J. Li, W. Xu, L. Wu, "Synthesis of flux switching permanent magnet machines", *IEEE Trans. Energy Convers.*, vol. 31, no. 1, pp. 106-117, Mar. 2016.

21. W. Hua, M. Cheng, Z. Q. Zhu, D. Howe, "Analysis and optimization of back EMF waveform of a flux-switching permanent magnet motor", *IEEE Trans. Energy Convers.*, vol. 23, no. 3, pp. 727-733, Sep. 2008.

22. Z. Xiang, X. Zhu, L. Quan, Y. Du, C. Zhang, D. Fan, "Multilevel design optimization and operation of a brushless double mechanical port flux-switching permanent-magnet motor", *IEEE Trans. Ind. Electron.*, vol. 63, no. 10, pp. 6042-6054, Oct. 2016.

23. G. Lei, W. Xu, J. Hu, J. Zhu, Y. Guo, K. Shao, "Multilevel design optimization of a FSPMM drive system by using sequential subspace optimization method", *IEEE Trans. Magn.*, vol. 50, no. 2, pp. 685-688, Feb. 2014.

24. H. Chen, X. Liu, A. M. EL-Refaie, J. Zhao, N. A. O. Demerdash, J. He, "Comparative study of winding configurations of a five-phase flux-switching PM machine", *IEEE Trans. Energy Convers.*.

25. S. J. Galioto, P. B. Reddy, A. M. EL-Refaie, J. P. Alexander, "Effect of magnet types on performance of high-speed spoke interior-permanent-magnet machines designed for traction applications", *IEEE Trans. Ind. Appl.*, vol. 51, no. 3, pp. 2148-2160, May 2015.

26. R. F. Schiferl, T. A. Lipo, "Power capability of salient pole permanent magnet synchronous motors in variable speed drive applications", *IEEE Trans. Ind. Appl.*, vol. 26, no. 1, pp. 115-123, Jan. 1990.

27. D. M. Ionel, M. Popescu, "Finite-element surrogate model for electric machines with revolving field-application to IPM motors", *IEEE Trans. Ind. Appl.*, vol. 46, no. 6, pp. 2424-2433, Nov. 2010.

28. Y. Duan, D. M. Ionel, "A review of recent developments in electrical machine design optimization methods with a permanent-magnet synchronous motor benchmark study", *IEEE Trans. Ind. Appl.*, vol. 49, no. 3, pp. 1268-1275, May 2013.

29. Z. Sun, J. Wang, G. W. Jewell, D. Howe, "Enhanced optimal torque control of fault-tolerant PM machine under flux-weakening operation", *IEEE Trans. Ind. Electron.*, vol. 57, no. 1, pp. 344-353, Jan. 2010.

30. A. M. EL-Refaie, "Fractional-slot concentrated-windings synchronous permanent magnet machines: Opportunities and challenges", *IEEE Trans. Ind. Electron.*, vol. 57, no. 1, pp. 107-121, Jan. 2010.

31. H. Chen, X. Liu, J. Zhao, N. A. O. Demerdash, "Magnetic-coupling characteristics investigation of a dual-rotor fault-tolerant PMSM", *IEEE Trans. Energy Convers.*, vol. 33, no. 1, pp. 362-372, Mar. 2018.

32. K. Price, R. M. Storn, J. A. Lampinen, Differential Evolution: A Practical Approach to Global Optimization, New York, NY, USA:Springer, 2006.

33. L. Shao et al., "Investigation on phase shift between multiple multiphase windings in flux-switching permanent magnet machines", *IEEE Trans. Ind. Appl.*, vol. 53, no. 3, pp. 1958-1970, May 2017.